

Electromagnetically Induced Transparency versus Nonlinear Faraday Effect. Coherent Control of the Light Beam Polarization

R. Drampyan

*Institute for Physical Research,
National Academy of Sciences of Armenia,
0203 Ashtarak-2, Armenia*

S. Pustelny, W. Gawlik

*Center for Magneto-Optical Research, Institute of Physics,
Jagiellonian University, Reymonta 4, 30-059 Kraków, Poland
(Dated: February 3, 2022)*

We report on experimental and theoretical study of the nonlinear Faraday effect under conditions of electromagnetically induced transparency at the $5S_{1/2} \rightarrow 5P_{3/2} \rightarrow 5D_{5/2}$ two-photon transition in rubidium vapors. These transitions realize the inverted Y model which combines the Λ and ladder systems. Strong nonlinearity allowing for large rotation angles of a probe beam tuned to the $S \rightarrow P$ transition was obtained by creation of quantum superpositions of magnetic sublevels (Zeeman coherences) in the rubidium ground state (Λ scheme). Additionally, electromagnetically induced transparency was accomplished in a ladder scheme by acting with an additional strong coupling laser on the $P \rightarrow D$ transition. Under conditions of a two-photon resonance the rotation was significantly reduced, which is interpreted as a competition between the two processes. The effect was observed in sub-Gauss magnetic fields and could be used for efficient coherent control of generation of the ground-state coherences, e.g. for controlling the polarization state of the probe light.

PACS numbers:

I. INTRODUCTION

Three-level atomic systems allow observation of several interesting and widely studied quantum-interference phenomena, such as coherent population trapping [1], electromagnetically induced transparency [2], electromagnetically induced absorption [3]. Extension of a number of levels and/or fields results in new effects related to double-dressing [4, 5], and interplay of coherences in the N [6, 7], tripod [8, 9], or inverted Y [10, 11] structures.

A specific example of quantum interference phenomenon is nonlinear magneto-optical rotation [12]. The effect is based on light-intensity dependent rotation of the polarization plane of linearly polarized light during its propagation through a medium subjected to the magnetic field. In this paper we address a special case of the phenomenon, the nonlinear Faraday effect (NFE) [13], which occurs in a magnetic field longitudinal to light propagation direction.

The rotation is associated with light-generated coherences between magnetic sublevels of atomic or molecular ground and/or excited states. NFE has thus the same physical mechanism as coherent population trapping (CPT) and the advantage of better signal-to-noise ratio over transmission measurements performed in most of the CPT experiments. A typical NFE signal recorded versus magnetic field is characterized by a dispersive shape centered at zero field with the width and amplitude determined by the relaxation rate of the coherences. Particularly large rotations (up to 100 mrad) can be observed when the coherences are established between mag-

netic sublevels of long-lived ground state. Application of anti-relaxation coating of gas container inner walls or introduction of a buffer gas into the vapor cell allow observation of extremely narrow, i.e. sub- μG , NFE signals associated with coherences of 100-ms or longer lifetimes [12, 14]. Another quantum interference phenomenon relevant for our research is electromagnetically induced transparency (EIT). The effect consists in reduction of the absorption of a weak, resonant probe light propagating through a medium in which the probe and a strong coupling beam jointly establish two-photon coherence in the three-level system. EIT may be observed in several three-level structures: Λ [15, 16], V [17] and ladder [18, 19]. EIT, as well as CPT are often used for inducing narrow transparency windows in otherwise optically dense samples and/or generating steep dispersion responsible for drastic modifications of the speed of light [16, 20, 21].

In this paper we analyze coexistence and competition between two different effect related with atomic coherences: NFE and EIT. Despite the fact that NFE is associated with ground-state coherences and EIT with coherences in a ladder scheme, they share intermediate excited levels and effectively affect one another. Interplay between the phenomena makes it possible to perform efficient all-optical coherent control over the polarization rotation. The NFE signals are analyzed for different probe and coupling-beam parameters and magnetic field strengths. Experimental data is supported by a theoretical model qualitatively explaining the observed characteristics.

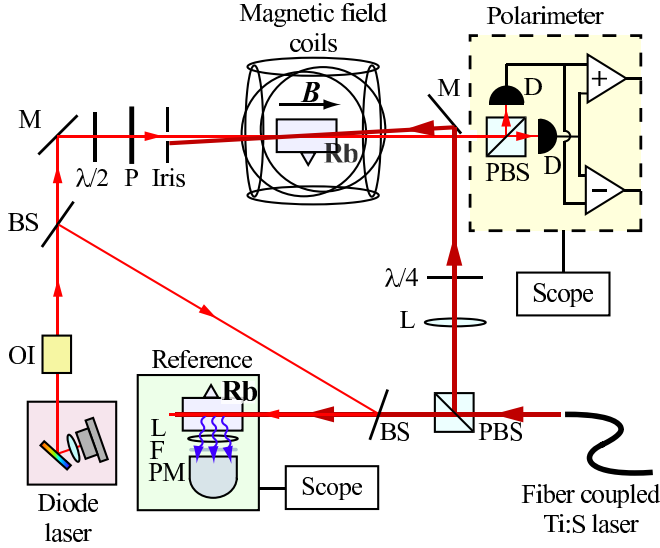


FIG. 1: Experimental apparatus. Two counter-propagating laser beams tuned to $5S_{1/2} \rightarrow 5P_{3/2}$ (probe light) and $5P_{3/2} \rightarrow 5D_{5/2}$ (coupling light) transition interact with rubidium atoms subjected to longitudinal magnetic field. The probe light is generated by an external-cavity diode laser, while the coupling light is provided by fiber-coupled titanium sapphire laser (Ti:S). OI denotes optical isolator, BS beam splitter, PBS polarizing beam splitter, M mirror, L lens, F interference filter, $\lambda/2$ and $\lambda/4$ are half-wave and quarter-wave plates, respectively, Rb is the rubidium vapor cell, PM photomultiplier, and D photodiodes.

Our approach significantly differs from the previous experiments on coherent control of optical rotation [22, 23, 24, 25, 26]. In particular, in Refs. [22, 23, 24] no magnetic field was used and the rotation arose exclusively due to light-induced birefringence of the medium. Wielandy *et al.* [25] and Padney *et al.* [26] did apply magnetic field but it was much stronger (~ 10 G) than in our work, therefore the NFE observed in Refs. [25, 26] was due to the excited- rather than ground-state coherences. Below, we demonstrate that involving the ground-state coherences results in an effective control by sub-Gauss magnetic fields.

The paper is organized as follows. In Sec. II the experimental arrangement is described. Experimental results are discussed in Sec. III. Section IV presents theoretical interpretation of the observed effects which are summarized in Sec. V.

II. EXPERIMENTAL APPARATUS

Experimental arrangement is shown in Fig. 1. Two counter-propagating beams: weak probe and strong coupling beam of 1 and 3 mm diameters, respectively, were overlapped in a rubidium vapor cell. The 4-cm long, 2.5-cm diameter cell contained natural mixture of rubidium with neither buffer gas nor wall coating. The probe light

emitted from the external-cavity diode laser (~ 1 MHz linewidth) was tuned to a particular hyperfine transition of the rubidium $D2$ line ($5S_{1/2} \rightarrow 5P_{3/2}$ transition of 780 nm wavelength and 5.8 MHz natural linewidth) or scanned across the whole Doppler-broadened $D2$ line. The probe beam was linearly polarized and its power was between 75 and 750 μW . The coupling beam emitted from a CW titanium sapphire laser (~ 3 MHz linewidth) was tuned to the $5P_{3/2} \rightarrow 5D_{5/2}$ transition corresponding to 776 nm wavelength and 0.97 MHz natural linewidth and its power was varied up to 30 mW. The corresponding energy level structure is shown in Fig. 2.

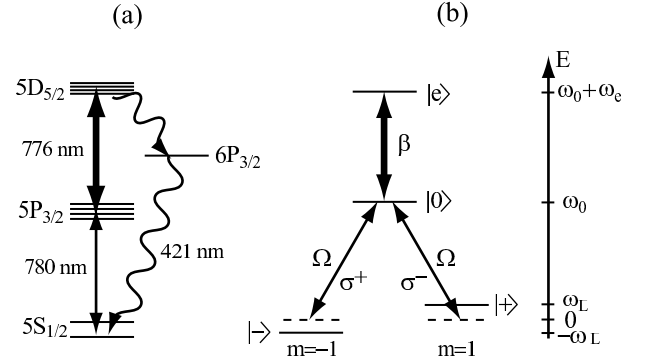


FIG. 2: Rubidium energy level structure (a) and inverted Y model used for theoretical analysis (b). Linearly polarized probe light was tuned to the $5S_{1/2} \rightarrow 5P_{3/2}$ transition while the strong coupling beam excited atoms at the $5P_{3/2} \rightarrow 5D_{5/2}$ transition. The atoms deexcited from the $5D_{5/2}$ state to the $5S_{1/2}$ state via intermediate state $6P_{3/2}$. Decay of the $6P_{3/2}$ state was accompanied with emission of blue light (421 nm) which was monitored in our experiment and used as reference.

Polarization of the coupling beam was set either linear or circular by a $\lambda/4$ waveplate. The counter-propagating arrangement of the probe and coupling beams provided that the two-photon interaction between the $5S_{1/2}$ and $5D_{5/2}$ states was possible only for a specific atomic velocity class which allowed observation of Doppler-free spectral features. The second rubidium cell was illuminated with co-propagating fractions of the probe and coupling beams and equipped with an interference filter and photomultiplier. It served as a reference for the two-photon resonance by monitoring the 421 nm fluorescence associated with deexcitation of the $5D$ levels in the $5D_{5/2} \rightarrow 6P_{1/2} \rightarrow 5S_{1/2}$ cascade (Fig. 2). The main rubidium cell was kept at room temperature (20°C) that corresponded to atomic density of $\sim 10^{10} \text{ cm}^{-3}$ and a Doppler width of ~ 0.5 GHz. The cell was surrounded by three orthogonal pairs of Helmholtz coils which compensated stray magnetic fields. The same coils were used for generation of an additional bias field in the range of -3 G to 3 G along the laser-beam direction.

The probe beam rotation was measured with a balanced polarimeter, i.e., a high-quality crystal polarizer and two photodiodes detecting intensities of two beams

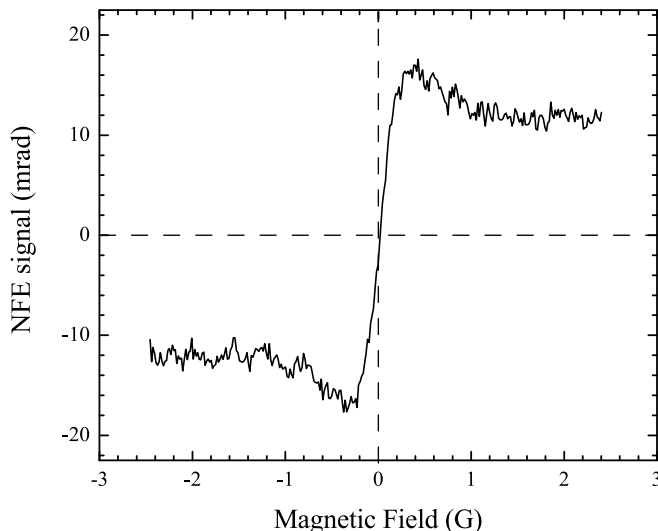


FIG. 3: NFE signal measured vs. longitudinal magnetic field. The signal was measured with the probe beam power of $75\ \mu\text{W}$ tuned to the center of the $F = 3 \rightarrow F'$ component of the D2 line in ^{85}Rb , and no coupling beam.

emerging from the polarizer. Analysis of the signals from two photodiodes yielded the angle of polarization rotation and transmitted signal power. In the described experiment, the rotation signals were recorded as functions of a longitudinal magnetic field B at fixed laser frequencies, or as functions of the probe frequency for fixed tuning of the coupling laser and constant magnetic field (usually about 70 mG).

III. RESULTS

A. NFE without coupling beam

The measurements started with recording of the probe-light polarization rotation versus the longitudinal magnetic field in absence of the coupling light. A typical signal measured under such conditions is shown in Fig. 3. It is characterized by an asymmetric curve of 20-mrad amplitude and a width of ~ 400 mG around $B = 0$. In a buffer-gas-free uncoated vapor cell, such as used in this work, the ground-state relaxation rate and hence the width of NFE resonance at low laser power equals to the inverse transit-time of atoms across the light beam. Under our experimental conditions the transit relaxation time was on the order of a few μs which roughly corresponds to a width of 200 mG. The difference between this number and experimentally observed width is attributed to power broadening caused by the $75\ \mu\text{W}$ probe light. The resonance presented in Fig. 3 has a shape which results from superposition of several nested dispersive contributions associated with Zeeman coherences in the ground and excited states, which are all centered at $B = 0$ but have different widths. Without the coupling

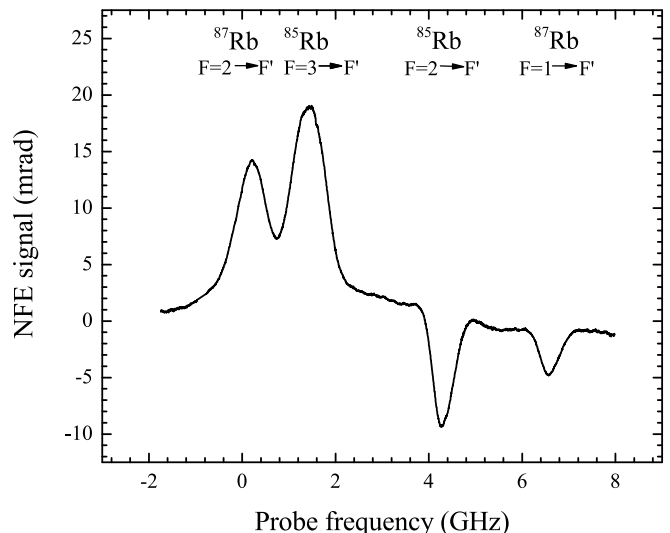


FIG. 4: NFE spectrum recorded at $B = 67$ mG without the coupling beam. The probe laser of $750\ \mu\text{W}$ was scanned around the hyperfine components with $F=2$ and $F=3$ of the D2 line of ^{87}Rb and ^{85}Rb , respectively.

beam the rotation spectra, i.e. NFE signal recorded versus the probe beam frequency ω_p at non-zero magnetic field ($B \neq 0$), are Doppler-broadened curves centered at hyperfine and isotope components of the investigated line (Fig. 4). For light power of $750\ \mu\text{W}$ the rotation reaches 20 mrad already at $B = 67$ mG which illustrates strong magnetic-field dependence of NFE, and maximizes at about 0.5 G at a level of a few tens of mrad. In such a case, however, the NFE signals could be contaminated by excited-state coherence (see discussion in Sec. IV), so the measurements were performed for $B < 100$ mG.

B. NFE with a coupling beam

After establishing main properties of the single-beam NFE, a series of NFE spectra with presence of the coupling beam was recorded. For these measurements the probe-light frequency was scanned across the D2 line while the coupling beam was tuned to the $5P_{3/2} \rightarrow 5D_{5/2}$ transition. NFE spectra measured with $500\ \mu\text{W}$ probe and 30 mW coupling beams and magnetic fields of $B = \pm 67$ mG are shown in Fig. 5. Doppler-broadened signals were observed at transitions associated with the resolved hyperfine structure of the ground states of both isotopes of rubidium, $F = 2 \rightarrow F'$ and $F = 1 \rightarrow F'$ for ^{87}Rb and $F = 3 \rightarrow F'$ and $F = 2 \rightarrow F'$ for ^{85}Rb , where F' denote unresolved excited-state hyperfine structure components. Reversing direction of the magnetic field changed signs of the observed dependence (Fig. 5), which was consistent with the change of the sign of rotation seen in Fig. 3. Small overall background observed for both spectra was related to imperfection of our polarimeter which resulted in residual polarization rotation.

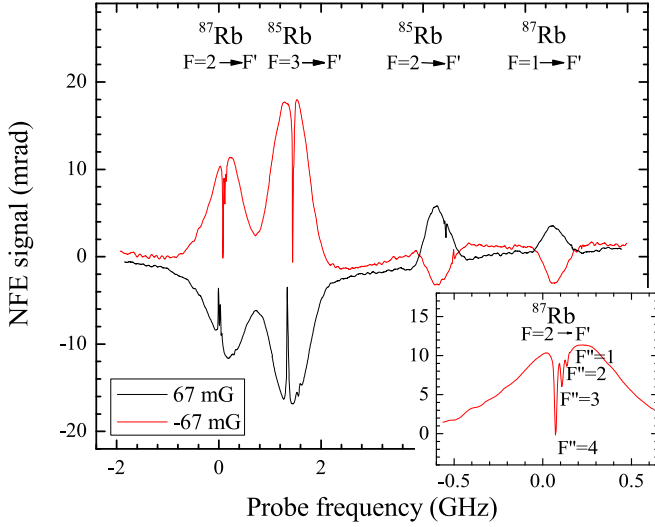


FIG. 5: Typical NFE spectra obtained with fixed frequency of the coupling laser and the probe light scanned across the rubidium D_2 line. The spectra consist of Doppler-broadened resonances and narrow spectral features. Inset shows the zoomed $F = 2 \rightarrow F'$ transition of ^{87}Rb and reveals dips corresponding to excited-state hyperfine structure. The spectra were recorded with 500 μW probe power and 30 mW coupling power.

While hyperfine structure of the excited states was not resolved with a single probe beam (Fig. 4), application of a counter-propagating coupling beam resulted in distinct Doppler-free dips related to EIT (Fig. 5). They were nearly 100% deep at the $F = 2 \rightarrow F'$ transition of ^{87}Rb and $F = 3 \rightarrow F'$ transition of ^{85}Rb , but weaker dips were also observed at the $F = 2 \rightarrow F'$ transition of ^{85}Rb .

In a gas sample, the EIT-induced spectral features can be observed only when the probe and the coupling beams simultaneously meet the resonance conditions

$$\begin{aligned}\omega_p + \mathbf{k}_p \cdot \mathbf{v} &= \omega_p^0, \\ \omega_c + \mathbf{k}_c \cdot \mathbf{v} &= \omega_c^0,\end{aligned}\quad (1)$$

where \mathbf{k}_p (\mathbf{k}_c) denotes the probe (coupling) light wave vector, \mathbf{v} is the atomic velocity, and ω_p^0 (ω_c^0) is the central frequency of the $5S_{1/2} \rightarrow 5P_{3/2}$ ($5P_{3/2} \rightarrow 5D_{5/2}$) line. For counter-propagating beams ($\mathbf{k}_p \approx -\mathbf{k}_c$), observation of the dips implies that the probe-light frequency fulfills the relation

$$\omega_p = \omega_p^0 + \frac{k_p}{k_c}(\omega_c^0 - \omega_c). \quad (2)$$

With fixed coupling-light frequency and the probe scanned across the transitions, the Doppler-free dips reveal hyperfine structure of the top state of the ladder structure (the $5D_{5/2}$ state). Inset to Fig. 5 presents the well resolved hyperfine structure of the $5D_{5/2}$ state of ^{87}Rb with about 30 MHz spacings between neighboring components. At the same time the hyperfine structure of the ^{85}Rb $5D_{5/2}$ level remains unresolved within the

$F = 3 \rightarrow F'$ line, which is the consequence of a much smaller hyperfine splitting of that state relative to the $5D_{5/2}$ state of ^{87}Rb .

Exact positions of the EIT dips and their assignments to specific hyperfine components depend on particular tuning of the coupling beam. For example, the NFE spectrum of ^{85}Rb shown in Fig. 5, reveals different positions of the Doppler-free EIT dips relative to the broad line centers. It can be explained by taking into account different tunings of the coupling beam with respect to the strongest transition within the Doppler-broadened line. In particular, the spectrum shown in Fig. 5 was taken with the coupling light tuned close to the center of the $F' = 4 \rightarrow F'' = 5$ transition which, according to Eq. (2), implies probe light to be tuned to the $F = 3 \rightarrow F' = 4$ transition for efficient EIT generation. Since this transition determines the position of the Doppler-broadened line, very deep dip appeared nearly at the center of broad line $F = 3 \rightarrow F'$. However, the same coupling frequency is detuned by 121 MHz from $F' = 3 \rightarrow F'' = 4$ transition. Since the strongest component of the $F = 2 \rightarrow F'$ line is associated with the $F' = 3$ state, the dip was shifted with respect to the line center.

Having analyzed spectral characteristics of NFE with the coupling beam, we investigated probe-polarization rotation versus the coupling-beam power. Figure 6 presents such dependence measured for two strongest Doppler-broadened NFE lines, the $F = 2 \rightarrow F'$ transition of ^{87}Rb and $F = 3 \rightarrow F'$ of ^{85}Rb . For coupling light power below $P_c < 0.1$ mW, no EIT was created and no Doppler-free features were observed in the rotation spectra. However, for higher coupling-beam powers, $P_c > 0.1$ mW, EIT became effective and resulted in appearance of Doppler-free dips within the spectrum. In particular, similarly as in inset to Fig. 5, well resolved features reflecting hyperfine structure of the excited state $5D_{5/2}$ were seen at the $F = 2 \rightarrow F'$ transition of ^{87}Rb . While the resonant dips reached nearly 100% contrast, their power broadening was very small within a range of applied light intensities.

Figure 7 presents NFE spectra measured with three different polarizations of the coupling beam, two opposite circular and linear polarizations with unchanged remaining experimental parameters. As shown, the spectra did not depend on the coupling-beam polarization. This point differs significantly from other measurements on coherent control of magneto-optical rotation [22, 23, 24, 25, 26] and indicates different nature of the rotation in our experiment than in previous studied cases. While in our experiment rotation was due to ground-state coherences, in earlier works it was caused by excited-state coherences and/or populations. This problem is addressed in more detail in Sec. IV.

Experimental study were completed with the series of measurements of NFE signals versus magnetic field for fixed probe frequency ω_p and different coupling-beam detunings (Fig. 8). As seen, the amplitude of the signal deteriorates when the coupling light is tuned to the two-

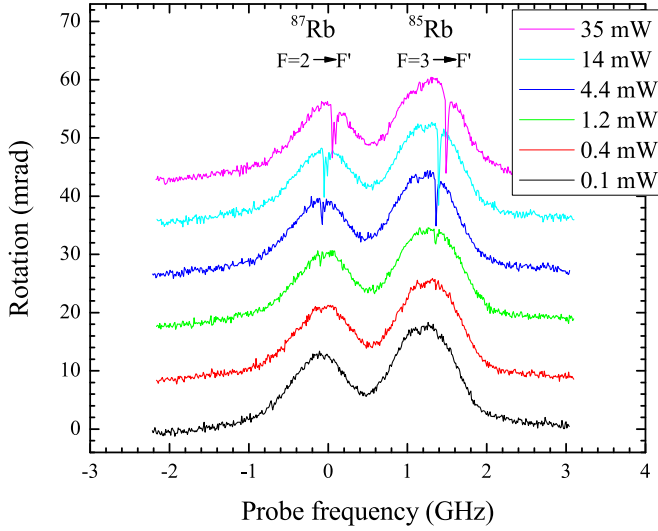


FIG. 6: Dependence of the probe-beam NFE spectra on the coupling-light power for the $F = 2 \rightarrow F'$ (^{87}Rb) and $F = 3 \rightarrow F'$ (^{85}Rb) components of the spectrum shown in Fig. 5. For low power no Doppler-free dips are visible. For coupling-beam powers higher than 1 mW, Doppler-free resonances show-up due to EIT. For each spectrum the coupling-light frequency was detuned from the resonance which resulted in frequency shifts of the observed Doppler-free features. For clarity, the signals were vertically displaced. The spectra were recorded with $B = 67$ mG.

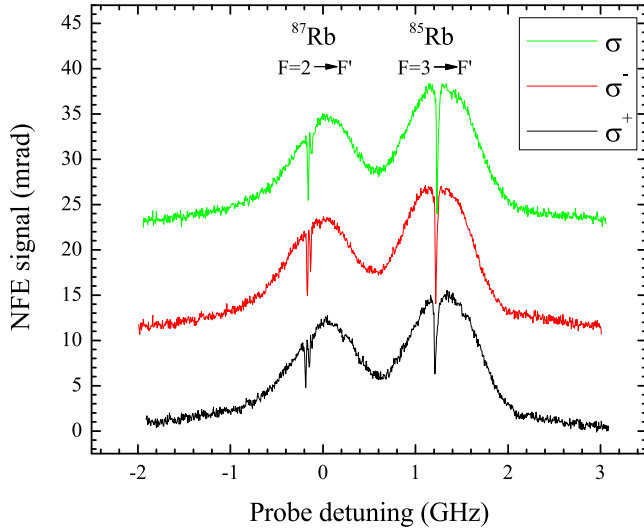


FIG. 7: NFE spectra vs. probe-light frequency for different polarizations of the coupling beam. The spectra, in particular, the Doppler-free dips associated with EIT, did not depend on coupling-beam polarization. The measurements were performed with $750 \mu\text{W}$ probe power, 14 mW coupling-beam power, and a magnetic field of 67 mG. For clarity the signals for σ^+ and σ^- polarizations were vertically shifted.

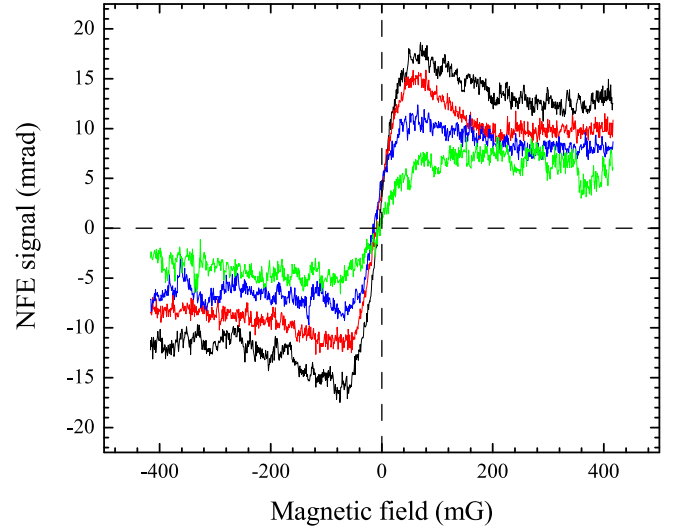


FIG. 8: NFE signal vs. magnetic field for different tunings of the coupling beam. Polarization rotation was the strongest when probe and coupling beams interacted with atoms from different velocity classes, i.e., when conditions given by Eqs. (1) were not fulfilled (black curve). The amplitude of the signal deteriorated when the beams started to generate EIT between ground and excited states. The strongest suppression of the signal were observed for the probe and coupling beams fulfilling the resonance conditions and interacting with the same atoms (green curve). The signals were measured with $750 \mu\text{W}$ -probe tuned to the center of the $F = 3 \rightarrow F'$ transition of ^{85}Rb and ~ 15 mW power of the coupling beam.

photon resonance. Specifically, it was almost three times smaller for the coupling beam in resonance, i.e., when both beams fulfilled the conditions given by Eqs. (1), than for far detuned coupling light. This reduction of the NFE signal amplitude is another manifestation of the competition between two processes of coherences generation. Fulfilling the two-photon resonance condition with appropriately strong coupling beam triggers EIT which strongly modifies efficiency of ground-state coherence generation and reduces the observed signal.

IV. THEORETICAL ANALYSIS

Although rubidium energy levels involved in our experiment form a fairly complex scheme [Fig. 2(a)], all salient features of our results can be interpreted in a much simpler *inverted Y* model system depicted in Fig. 2(b). It enables simple analytical solutions of the density matrix and provides very good physical insight into the problem. The model system consists of a ground state with two Zeeman components corresponding to $m = \pm 1$ (states $|\pm\rangle$) which are split in the external magnetic field B by $2\omega_L$, and two excited states, one labelled as $|0\rangle$ coupled with $|+\rangle$ and $|-\rangle$ by a linearly polarized probe beam, and state $|e\rangle$ which is linked with $|0\rangle$ by a strong coupling

beam. Without the coupling beam the model represents Λ system which is a generic structure not only for NFE, but also other CPT-like phenomena. With just one of the ground-state sublevels, the model becomes a familiar ladder EIT scheme. Simultaneous presence of two light beams and a magnetic field allows interplay of both these effects. Our analysis differs from earlier work on inverted Y scheme by Joshi and Xiao [10] as it employs two, rather than three laser beams in a combination of the ladder system and the Λ system which involves Zeeman sublevels in the lower state. The latter system allows control of the atomic coherence by a magnetic field.

We performed analysis of the experiment using the density-matrix formalism in which the evolution of the density operator ϱ is described by the Liouville equation

$$\dot{\varrho} = -\frac{i}{\hbar}[H, \varrho] + \frac{1}{2}\{\Gamma, \varrho\} + \Lambda, \quad (3)$$

where $[\ , \]$ denotes commutator, $\{\ , \ \}$ anticommutator, H the full Hamiltonian of the system, while Γ and Λ represent the relaxation and pumping operators, respectively, responsible for retaining the thermal equilibrium populations of the unperturbed system. In our analysis we took hamiltonian H as

$$H = H_0 - \boldsymbol{\mu} \cdot \mathbf{B} - \mathbf{E} \cdot \mathbf{d}, \quad (4)$$

where H_0 is unperturbed Hamiltonian of the system, \mathbf{d} denotes electric and $\boldsymbol{\mu}$ magnetic dipole moment operators, and \mathbf{E} is the electric field of light taken in the form

$$\mathbf{E} = (\mathbf{e}_+ + \mathbf{e}_-)E_p e^{i\omega_p t} + \mathbf{e}_e E_e e^{i\omega_e t}, \quad (5)$$

with \mathbf{e}_i are respective polarization vectors.

Within the rotating wave approximation, the model system can be described by the following set of equations for slowly-varying envelopes σ of the density matrix elements.

$$\begin{aligned} \dot{\rho}_{\pm\pm} &= -i\Omega(\sigma_{\pm 0} - \sigma_{0\pm}) - \gamma(\rho_{\pm\pm} - N) + \frac{\Gamma_0}{2}\rho_{00}, \\ \dot{\rho}_{00} &= i\Omega(\sigma_{+0} - \sigma_{0+} + \sigma_{-0} - \sigma_{0-}) - i\beta(\sigma_{0e} - \sigma_{e0}) \\ &\quad - \Gamma_0\rho_{00} + \Gamma_e\rho_{ee}, \\ \dot{\rho}_{ee} &= i\beta(\sigma_{0e} - \sigma_{e0}) - \Gamma_e\rho_{ee}, \\ \dot{\sigma}_{\pm 0} &= -iA_{\pm}\sigma_{\pm 0} + i\Omega(\rho_{00} - \rho_{\pm\pm} - \sigma_{\pm\mp}) - i\beta\sigma_{\mp e}, \\ \dot{\sigma}_{-+} &= iB\sigma_{-+} + i\Omega(\sigma_{0+} - \sigma_{-0}), \\ \dot{\sigma}_{0e} &= -iK\sigma_{0e} + i\Omega(\sigma_{-e} + \sigma_{+e}) + i\beta(\rho_{ee} - \rho_{00}), \\ \dot{\sigma}_{\pm e} &= -iC_{\pm}\sigma_{\pm e} + i\Omega\sigma_{0e} - i\beta\sigma_{\pm 0}. \end{aligned} \quad (6)$$

with

$$\begin{aligned} A_{\pm} &= \Delta\omega_0 \pm \omega_L - i\gamma_{\pm 0}, \\ K &= 2\omega_L + i\gamma_{-+}, \\ C_{\pm} &= \Delta\omega_0 + \Delta\omega_e \pm \omega_L - i\gamma_{\pm e}, \\ M &= \Delta\omega_e - i\gamma_{0e}, \end{aligned} \quad (7)$$

where γ_{ik} denote the relaxation rates of the σ_{ik} coherences ($i, k = \pm, 0, e$), γ is the relaxation rate of the

ground-state population, Γ_0 the spontaneous emission rate of state $|0\rangle$, and Γ_e of state $|e\rangle$, $\Delta\omega_0$ and $\Delta\omega_e$ are detuning of the probe and coupling beams from respective transitions at zero magnetic field, ω_L is the Larmor frequency, Ω and β are the Rabi frequencies of the probe and coupling beams, and N denotes the unperturbed equilibrium populations of the ground states. Equations (6) solved within the steady-state approximation yield

$$\begin{aligned} \sigma_{\pm 0} &= -\frac{\Omega}{A_{\pm}}(N + \sigma_{\pm\mp}) - \frac{\beta}{A_{\pm}}\sigma_{\pm e}, \\ \sigma_{-+} &= \frac{\Omega}{K}(\sigma_{-0} - \sigma_{0+}), \\ \sigma_{0e} &= \frac{\Omega}{M}(\sigma_{-e} + \sigma_{+e}), \\ \sigma_{\pm e} &= -\frac{\beta}{C_{\pm}}\sigma_{\pm 0}, \end{aligned} \quad (8)$$

where the probe-beam Rabi frequency Ω was assumed to be much smaller than the excite-state relaxation rate Γ_0 , ($\Gamma_0 \ll \Omega$) but stronger than the relaxation rate of the ground state γ . It allows one to omit product $\Omega\sigma_{0e}$ in Eqs. (8) [27] and neglect optical pumping (within this approximation the populations of the levels did not depend on light intensity: $\rho_{\pm\pm} = N$ and $\rho_{00} = \rho_{ee} = 0$). These assumptions enable presentation of the optical coherences $\sigma_{\pm 0}$, as well as the σ_{-+} and $\sigma_{\pm e}$ coherences responsible for NFE and EIT in very simple analytical forms

$$\begin{aligned} \sigma_{\pm 0} &= \frac{\Omega K C_{\pm}}{D_{\pm}}(A_{\mp}^* C_{\mp}^* + \beta^2)N, \\ \sigma_{\pm e} &= -\frac{\Omega \beta K}{D_{\pm}}(A_{\mp}^* C_{\mp}^* - \beta^2)N, \\ \sigma_{-+} &= \frac{\Omega^2}{D_-} [C_- C_+^* (A_+^* - A_-) - \beta^2 (C_+^* - C_-)] N, \end{aligned} \quad (9)$$

where

$$\begin{aligned} D_{\pm} &= C_{\pm} C_{\mp}^* [A_{\pm} A_{\mp}^* K - \Omega^2 (A_{\pm} - A_{\mp}^*)] - \beta^2 K \times \\ &\quad \times (A_{\pm} C_{\pm} + A_{\mp}^* C_{\mp}^*) - \beta^2 \Omega^2 (C_{\pm} - C_{\mp}^*) + \beta^4 K. \end{aligned} \quad (10)$$

It should be noted that despite these simplification theoretical modeling based on Eqs. (9) are in very good agreement with experimental data. Taking into account optical pumping effects is quite straightforward with our model but does not change the overall character of the simulated results.

Equations (9) can be used for modelling various signals. For instance, in the transmission measurements the absorption coefficient for a single polarization component of the probe is determined by $\text{Im}\sigma_{\pm 0}$, in the magnetic dichroism measurement the signal is given by $\text{Im}(\sigma_{+0} - \sigma_{-0})$, and for detection of fluorescence its intensity is given by $\text{Im}(\sigma_{+0} + \sigma_{-0})$. For the rotation measurements, such as performed in this work, the Faraday rotation angle is proportional to the difference of the real parts of the optical coherences associated with the σ^+ and σ^- components of the probe field $\theta \propto \text{Re}(\sigma_{+0} - \sigma_{-0})$.

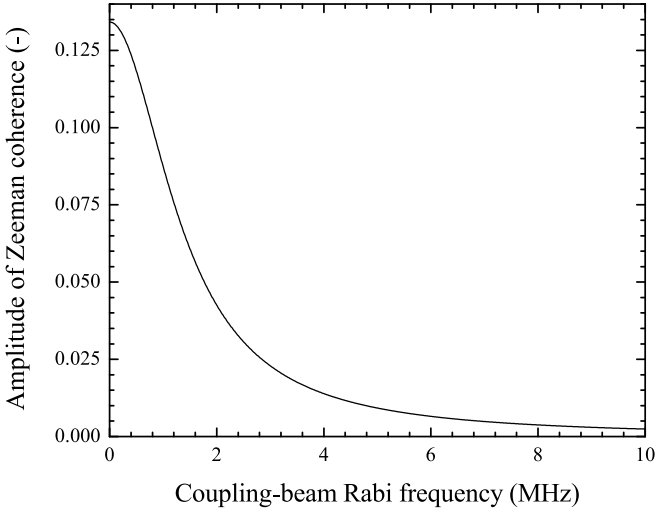


FIG. 9: Amplitude of the real part of the Zeeman coherences σ_{-+} as a function of the Rabi frequency of the coupling light β . Signals were simulated for both beams tuned to the resonance ($\Delta\omega_0 = \Delta\omega_e = 0$), probe-light Rabi frequency of 0.3 MHz, the Larmor frequency corresponding to the maximum of the NFE signal $\omega_L = 0.05$ MHz, and the equilibrium populations $N = 0.5$.

For $\beta = 0$, Eqs. (9) allow one to reproduce typical NFE signals such as depicted in Fig. 3. When the coupling laser is on ($\beta \neq 0$) but the magnetic field is off ($B = 0$), the formulae can be used for description of EIT on the degenerate $|\pm\rangle - |0\rangle$ transitions. When all perturbations are acting simultaneously ($\beta \neq 0$, $B \neq 0$), solutions (9) reproduce effects due to EIT and CPT, such as predicted by Joshi and Xiao [10] for transmission measurements. For the Faraday geometry, expressions (9) reflect competition between NFE and EIT which not only bleaches the weak probe absorption but also reduces nonlinear rotation of its polarization, as shown in Figs. 5-8. Figure 9 shows how the amplitude of the real part of the Zeeman coherence σ_{-+} is reduced by increasing Rabi frequency β of the coupling laser. Since this is the Zeeman coherence which is responsible for the nonlinear Faraday effect, this dependence explains the reduction of the rotation signal amplitude seen in the experiments with the coupling laser, i.e. when $\beta \neq 0$.

For the description of experiments with a vapor cell, the density matrix needs to be velocity averaged with the detunings of the counter-propagating probe and coupling laser beams modified to account for the Doppler shifts: $\Delta\omega_0 \rightarrow \Delta\omega_0 - kv_p \approx \Delta\omega_0 - kv$, $\Delta\omega_e \rightarrow \Delta\omega_e + kv_e \approx \Delta\omega_e + kv$, where v is the atomic speed along the laser beam directions and k the wavenumber. Figure 10 represents such averaged signals simulated with the inverted Y model for different coupled-beam detunings $\Delta\omega_e$ and scanned probe-laser detuning $\Delta\omega_e$. The theoretical rotation spectra agree very well with our observations. In particular, they exhibit Doppler-free dips which appear at two-photon resonance, i.e. when $\Delta\omega_0 + \Delta\omega_e = 0$

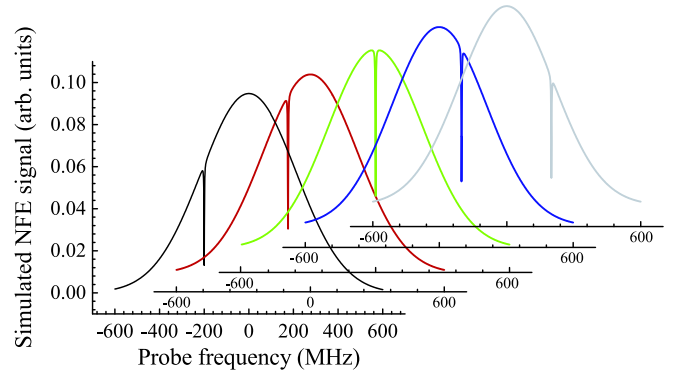


FIG. 10: Theoretical NFE spectra calculated for $\Delta\omega_0 = 0$ and different detunings of the coupling laser: $\Delta\omega_e = 200$ MHz (gray), 100 MHz (blue), 0 MHz (green), -100 MHz (red), and -200 MHz (black) from the bottom to the top curve, respectively. The signals were calculated for a Larmor frequency of 0.1 MHz, probe and coupling-light Rabi frequencies of $\Omega = 0.3$ MHz and $\beta = 3$ MHz, respectively.

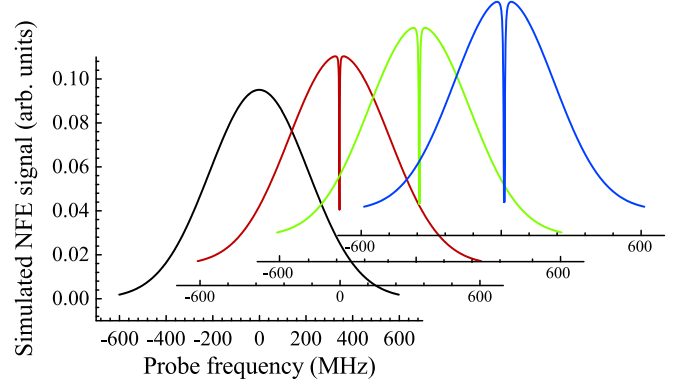


FIG. 11: NFE spectra simulated for different Rabi frequencies of the coupling laser, $\beta = 0, 3, 6$, and 9 MHz. The simulations were performed with Larmor frequency of 0.1 MHz, probe-light Rabi frequency of 0.3 MHz, and $\Delta\omega_0 = \Delta\omega_e = 0$.

(Fig. 10). If $\Delta\omega_e \neq 0$, the dips are shifted from $\Delta\omega_0 = 0$, as seen in the experimental spectra (Fig. 6). These dips have bigger contrast than regular ladder EIT resonances. The contrast increases with β which is demonstrated in Fig. 11 and agrees with the observation (Fig. 6). At the same time, power broadening of the EIT rotation dip is very small. These features may be useful for laser frequency stabilization, although the dip positions are not related directly to the atomic transitions but depend on particular $\Delta\omega_e$.

The effect of quenching the Zeeman coherence by a coupling laser illustrated in Fig. 9 is responsible for cancellation of the NFE signal. This effect is also very well reproduced by our model. Figure 12 presents a sequence of the rotation signals calculated for Doppler-averaged medium with fixed B and ω_p and for various values of $\Delta\omega_e$ which correspond to those in Fig. 8. The calculated signals reproduce very well the observed behavior

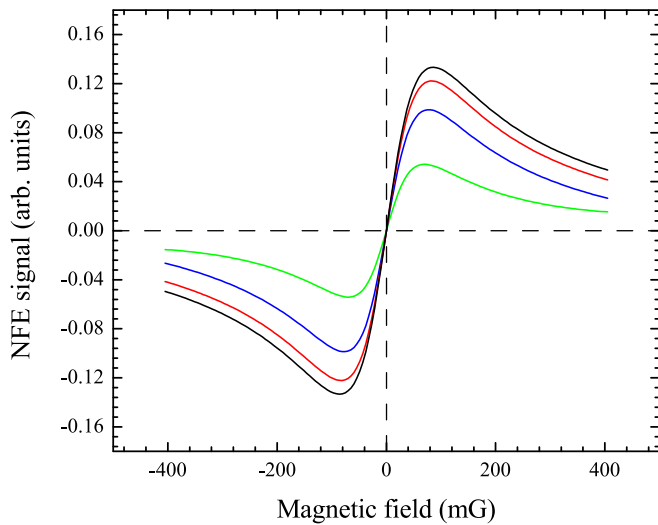


FIG. 12: NFE signals vs. magnetic field simulated for probe and coupling-beam Rabi frequencies of 0.3 MHz and 3 MHz, respectively and different detunings of the coupling beam which correspond to those in Fig. 8: $\Delta\omega_e = 0.6$ MHz (green), 1.3 MHz (blue), 2.0 MHz (red), and 2.7 MHz (black) which manifest by different amplitudes of magneto-optical rotation.

(Fig. 8).

In contrast to previous work on polarization control based on light-induced optical anisotropy [25, 26], the described changes of rotation do not depend on the coupling-beam polarization (Fig. 7). This difference is caused by the fact that in our study the optical anisotropy resulting in the rotation of the probe beam polarization reflects the ground-, rather than excited-state coherence. The inverted Y model, very successful in explaining most features observed in our experiment is quite insensitive to the polarization of the coupling-beam as this beam acts symmetrically on both transitions involving the lower Λ levels, hence it does not create any anisotropy of the probe-beam propagation.

It is important to notice that while the real energy-level structure of rubidium does possess many excited sublevels and many possible excited-state coherences, these are the ground-state coherences which dominate the probe-beam polarization rotation. This is because the rates of creation of the ground state observables (co-

herences and/or population redistribution) are by factor Γ_0/γ bigger than the corresponding rates for the excited state. Thus, if both coherences are allowed by the level structure, the ground-state ones make by far stronger impact onto the interaction dynamics (see, e.g., Ref. [28]). However, the contributions of the ground-state coherences to NFE signal have the form of very narrow resonances, which reflects that they are destroyed by fast precession in magnetic fields such that $\omega_L > \gamma_{-+}$. For larger fields, such that $\gamma_+ \ll \omega_L \approx \Gamma_0$, the ground-state coherences became irrelevant. Thus, for fields on the order of 10 G, the excited-state observables become important and the rotation depends on the coupling-beam polarization, as observed in experiments with stronger magnetic fields [25, 26].

V. CONCLUSIONS

We have studied nonlinear Faraday effect under conditions of electromagnetically induced transparency. It was experimentally discovered that the two coherent processes, NFE/CPT and EIT, compete which quenches the magneto-optical rotation. A theoretical description based on a simple inverted Y model reproduced all salient features of the observations and revealed detailed physical mechanism behind the observed behavior. The interplay between NFE and EIT allows one to perform coherent control of the polarization state in a different manner than in the previously proposed schemes. While the previous approaches were relying on excited-state coherences, the described method is based on the ground-state coherences which permits to use much weaker light beams and magnetic fields to obtain the desired control. The competition of NFE and EIT results in Doppler-free spectral features which have higher contrast than the regular EIT dips in a standard transmission measurements. In principle, the enhanced contrast may be useful for precision spectroscopy and/or laser-frequency stabilization.

Acknowledgments

This work was partly supported by the Polish Ministry of Science grants NN505092033 and NN202074135.

-
- [1] E. Arimondo, in *Progress in Optics* **35**, E. Wolf ed. (Elsevier Science, New York, 1996), 259-354.
 - [2] M. Fleischhauer, A. Imamoglu, J.P. Marangos, *Rev. Mod. Phys.* **77**, 633 (2005).
 - [3] A. M. Akulshin, S. Barreiro, A. Lezama, *Phys. Rev. A* **57** 2996 (1998).
 - [4] M.D. Lukin, S.F. Yelin, M. Fleischhauer, and M.O. Scully, *Phys. Rev. A* **60** 3225 (1999).
 - [5] G. Wąsik, W. Gawlik, J. Zachorowski, Z. Kowal, *Phys. Rev. A* **64**, 051802(R) (2001).
 - [6] S. R. de Echaniz, A. D. Greentree, A. V. Durrant, D. M. Segal, J. P. Marangos, J. A. Vaccaro, *Phys. Rev. A* **64**, 013812 (2001).
 - [7] C. Goren, A. D. Wilson-Gordon, M. Rosenbluh and H. Friedmann, *Phys. Rev. A* **69**, 053818 (2004).
 - [8] Z. Kis, F. Renzoni, *Phys. Rev. A* **65**, 032318 (2002).
 - [9] D. Petrosyan, Y. P. Malakyan, *Phys. Rev. A* **70**, 023822 (2004).
 - [10] A. Joshi and M. Xiao *Phys. Lett. A* **317**, 370 (2003);
 - [11] A. Joshi and M. Xiao *Phys. Rev. A* **72**, 062319 (2005).

- [12] D. Budker, W. Gawlik, K. F. Kimball, S. M. Rochester, V. V. Yashchuk, and A. Weis, *Rev. Mod. Phys.* **74**, 1153 (2002).
- [13] W. Gawlik, S. Pustelny, in *New Trends in Quantum Coherence and Nonlinear Optics*, R. Drampyan ed. (Nova Publishers, New York, 2009), pp. 47-84.
- [14] D. Budker, L. Hollberg, D. F. Kimball, J. Kitching, S. Pustelny, and V. V. Yashchuk, *Phys. Rev. A* **71**, 012903 (2005).
- [15] Y. Q. Li, M. Xiao, *Phys. Rev. A* **51**, 4959 (1995).
- [16] L. V. Hau, S. E. Harris, Z. Dutton, C. H. Behroozi, *Nature* **397**, 594 (1999).
- [17] J. R. Boon, E. Zekou, D. J. Fulton, M. H. Dunn, *Phys. Rev. A* **57**, 1323 (1998).
- [18] R. R. Moseley, S. Sheperd, D. J. Fulton, B. D. Sinclair, M. H. Dunn, *Opt. Commun.* **119**, 61 (1995).
- [19] J. J. Clarke, W. A. van Wijngaarden, H. Chen, *Phys. Rev. A* **64**, 023818 (2001).
- [20] A. Merriam, S. J. Sharpe, H. Xia, D. Manuszak, G. Y. Jin, S. E. Harris, *Opt. Lett.* **24**, 625 (1999).
- [21] D. Budker, D. F. Kimball, S. M. Rochester, V. V. Yashchuk, *Phys. Rev. Lett.* **83**, 1767 (1999).
- [22] P. F. Liao, G. C. Bjorklund, *Phys. Rev. Lett.* **36**, 584 (1976).
- [23] P. F. Liao, G. C. Bjorklund, *Phys. Rev. A* **15**, 2009 (1977).
- [24] F. S. Pavone, G. Bianchini, F. S. Cataliotti, T. W. Hänsch, M. Inguscio, *Opt. Lett.* **22**, 736 (1997).
- [25] S. Wielandy, A. L. Gaeta, *Phys. Rev. Lett.* **81**, 3359 (1998).
- [26] K. Pandey, A. Wasan, V. Natarajan, *J. Phys. B: At. Mol. Opt. Phys.* **41**, 225503 (2008).
- [27] J. Gea-Banacloche, Y. Q. Li, S. Z. Jin, M. Xiao, *Phys. Rev. A* **51**, 576 (1995).
- [28] W. Gawlik, *Acta Phys. Polon. A* **66**, 401 (1984).